

# RF-Bouncer: A Programmable Dual-band Metasurface for Sub-6 Wireless Networks

Xinyi Li<sup>1,\*</sup>, Chao Feng<sup>1,\*</sup>, Xiaojing Wang<sup>1</sup>, Yangfan Zhang<sup>1</sup>, Yaxiong Xie<sup>2</sup>, Xiaojiang Chen<sup>1,†</sup>

<sup>1</sup>Northwest University, <sup>2</sup>University at Buffalo SUNY

## Abstract

Offloading the beamforming task from the endpoints to the metasurface installed in the propagation environment has attracted significant attention. Currently, most of the metasurface-based beamforming solutions are designed and optimized for operation on a single ISM band (either 2.4 GHz or 5 GHz). In this paper, we propose RF-Bouncer, a compact, low-cost, simple-structure programmable dual-band metasurface that supports concurrent beamforming on two Sub-6 ISM bands. By configuring the states of the meta-atoms, the metasurface is able to simultaneously steer the incident signals from two bands towards their desired departure angles. We fabricate the metasurface and validate its performance via extensive experiments. Experimental results demonstrate that RF-Bouncer achieves 15.4 dB average signal strength improvement and a 2.49× throughput improvement even with a relatively small 16 × 16 array of meta-atoms.

## 1 Introduction

It is a common practice for wireless communication systems to leverage beamforming technique to improve the throughput and extend the communication range. Higher beamforming gain requires a larger number of antennas installed on the communication endpoints. Two practical challenges hinder the deployment of radio systems with a large antenna array. First, the majority of today's IoT devices have to be small in size due to cost and form factor constraints, leaving no space for a large array. Second, the radio chains connected to each antenna increase hardware costs and power consumption.

Recently, offloading the beamforming from the communication endpoints to a metasurface deployed in the propagation environment has attracted significant attention [4, 14]. RFocus [4] leverages a metasurface that consists of thousands of simple 2-way RF switches to beamform the incoming signal towards the receiver. Due to the limited programmability of

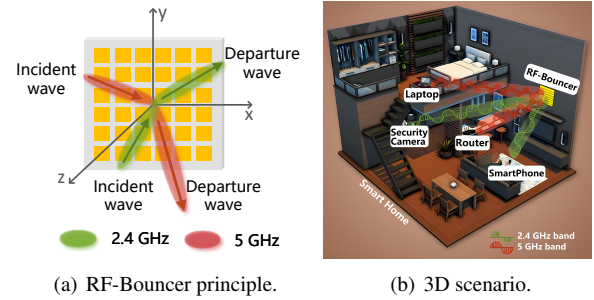


Figure 1: RF-Bouncer's metasurface simultaneously steers the incident signal towards the target directions at two bands, improving the overall performance of dual-band concurrent communication in a complex 3D indoor environment.

the RF switch, *i.e.*, switch on for reflecting and switch off for no reflection, RFocus needs huge number of meta-atoms to work efficiently and robustly. RFlens [14] upgrades the metasurface with a dedicated meta-atom that resembles a 1-bit phase shifter and thus achieves reasonable beamforming performance with only 256 functional meta-atoms.

We observe that most of the current metasurface-based beamforming solutions focus on optimizing communication performance on single frequency band, for example, RFocus works for frequencies below 3 GHz while RFlens is optimized for 5 GHz band. But, these two Sub-6 ISM bands at 2.4 GHz and 5 GHz accommodate three wireless protocols widely used for communication between IoT devices: Wi-Fi, Bluetooth and ZigBee. Due to the densely deployed IoT devices, concurrent wireless transmissions over two Sub-6 ISM bands are very common. A naive solution to extend existing solutions to support dual-band operation is to install two meta-surfaces, one for a single band. Such a solution not only requires more deployment space to accommodate the extra metasurfaces but also results in higher costs. Stacking one metasurface on top of another [42] is another option to support the dual-band operation, resulting in a complicated circuit design. More recent attempts [11, 14, 26, 32] employ varactor to adjust phase, which incurs a high insertion loss [26, 32] and require a precise

\*Co-primary authors, both authors contributed equally to this research.

†Corresponding author.

and sophisticated DC voltage control backend [11, 14].

In this paper, we propose to design an area-efficient, low-cost, and simple-structure programmable dual-band metasurface that supports concurrent beamforming on two ISM bands. By concurrent beamforming we mean the metasurface is able to simultaneously steer the two incident signals from two ISM bands towards their desired departure angles, just as shown in Figure 1. The locations of the two pairs of transceivers are random in practice, so our metasurface should work with an arbitrary combination of two incident angles and two departure angles in 3-D space, as shown in Figure 1 (b).

Designing a dual-band metasurface is challenging. Generally, to maximize the communication efficiency, the electric length of the RF components (meta-atoms) should match the wavelength of the signal. There exists a large discrepancy in the wavelength of signals from two widely separated bands, for example, the wavelength is 12 cm and 6 cm for signals at frequency 2.4 GHz and 5 GHz, respectively. Therefore, it is difficult to fabricate hardware with fixed physical dimensions but multiple resonance frequencies.

To solve the problem, we propose a novel meta-atom that has two resonant frequencies (bi-resonant), by integrating two antenna structures. The basic structure of our meta-atom is a metal-backed patch square structure. By adjusting its physical dimensions, we successfully fix its resonant frequency to the first ISM band (2.4 GHz). To generate an additional resonant frequency, we propose to etch slots on the patch, since the slots impact the path of the stimulated current and thus the resonant frequency, according to antenna theory [5]. By fine-tuning the location, the number and the physical dimensions of the slots on the patch, we successfully generate the second resonant frequency at the second ISM band (5 GHz) without affecting the first resonant frequency.

To empower the meta-atoms with dual-band programmability, we embed two PIN diodes into carefully selected positions of the patch on the meta-atom. Each PIN diode functions similarly to an RF switch, and two PIN diodes provide four "on/off" states. Depending on the state of the PIN diodes, the meta-atom introduces different amount of phase shifts to its reflected signal, resembling a 2-bit phase shifter.

Based on our programmable dual-band metasurface, we implement a dual-band beamforming algorithm that can quickly configure the states of all meta-atoms to accurately steer the incident signal towards the desired departure angle. We also design a beam alignment algorithm to adjust the configurations of meta-atoms in real-time to handle user mobility.

We build a prototype of RF-Bouncer's metasurface by embedding  $16 \times 16$  meta-atoms inside an area of  $0.35 \times 0.35 m^2$ . Owing to its small form factor, RF-Bouncer's metasurface can be attached to the facades of the ambient environment such as walls, furniture, and advertisement boards. Hence, RF-Bouncer can easily cope with complex indoor environments, as shown in Figure 1. Extensive experiments demonstrate that even with the small-size prototype, RF-Bouncer enables

15.4 dB average signal strength improvement and a  $2.49 \times$  throughput improvement. RF-Bouncer also works robustly across protocols (e.g., Bluetooth, Zigbee and Wi-Fi), and in complex radio environments (3D and even NLoS).

**Contributions.** The main contributions of RF-Bouncer are: (i) We design a programmable dual-band metasurface that supports concurrent beamforming over two ISM bands<sup>1</sup>. (ii) We implement a dual-band beamforming algorithm that can quickly configure the metasurface to simultaneously steer the incident signals of two bands towards their desired departure directions. (iii) We fabricate RF-Bouncer's metasurface and validate its effectiveness in a wide range of practical scenarios.

## 2 Related Work

**Metasurfaces and smart surfaces.** Metasurfaces are three-dimensional, periodic, and artificial structures [6, 10, 17, 30]. By manipulating the phase/ amplitude of electromagnetic waves, it can beamform or re-steer the signals towards an intended direction, so as to extend the network coverage. MilliMirror [28] utilizes a 3D printed metasurface to re-steer mmWave beams to illuminate coverage blind spots. Although promising, such metasurfaces are not configurable. To enable programmability, prior studies focus on adding electronic components (i.e., varactors [8, 12, 15] or PIN diodes [35, 40, 41]) into the metasurface. Another line of literature improves indoor network coverage by designing and deploying smart surfaces in the environment to manipulate wireless channels. These smart surfaces generally consist of non-periodic but adjustable electronic components [4, 13, 39]. While the above methods have shown great promise, they mostly focus on single-link optimizations and are not yet optimized for dual-band concurrent links or 3D coverage. Unlike them, RF-Bouncer aims to simultaneously support dual-band wireless links (e.g., 2.4 GHz and 5 GHz) and targets indoor 3D network coverage improvement.

**Expanding indoor wireless coverage.** To expand the wireless coverage, several systems [9, 16, 20, 27, 36] deploy passive reflectors near the AP to reflect the incident signal to enhance the link SNR. Such reflectors, however, cannot be re-configured, resulting that they cannot adapt to dynamic indoor environments. Instead, RF-Bouncer can dynamically configure the metasurface to reshape incident beams, thus adapting to dynamic indoor environments. Alternatively, some studies improve indoor wireless coverage by installing multiple APs [24, 25, 29, 34] or RF relays [2, 7, 18] in the environment. Yet, when applying to a new wireless standard or working frequency band, these approaches require updating protocols or hardware, which is cumbersome and high implementation cost. In contrast, RF-Bouncer is a standard-agnostic and cost-effective solution to enhance indoor wireless coverage.

---

<sup>1</sup>The design of RF-Bouncer is available at: [https://github.com/ZYF-PhD/RF-Bouncer\\_OpenSource](https://github.com/ZYF-PhD/RF-Bouncer_OpenSource)

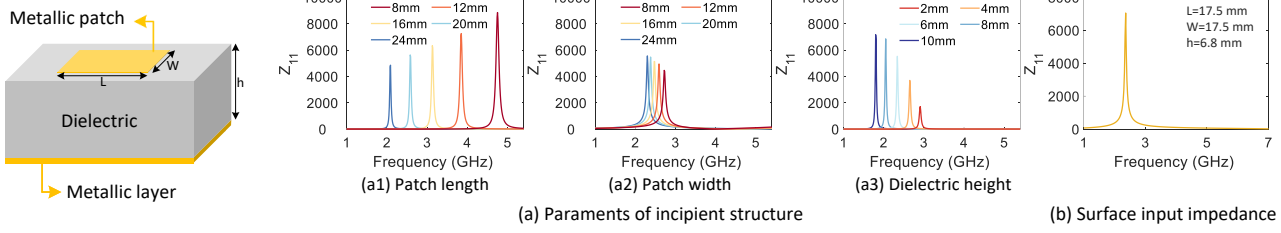


Figure 2: The incipient structure of meta-atom. Figure 3: Impact of the paraments of the incipient structure and the surface input impedance across operating frequencies.

**Dual-band design.** Many efforts have been devoted to designing dual-band metasurfaces. Stacking two metasurfaces with two resonant frequencies is a straightforward solution [42], which however results in complicated circuit design. Some studies [22, 37] exploit polarization orthogonality to enable dual-band reflectarray antenna, one polarization for each band, while RF-Bouncer supports dual-band with the same polarization, without requiring low-cost IoT devices to rotate when switching the working frequency bands. [23] propose a metasurface structure that supports dual-band but only produces two symmetrical reflected beams, lacking programmability in controlling the departure direction. Some recent attempts [11, 32] employ varactor to adjust phase, which incurs a high insertion loss [26, 32] and requires a precise and sophisticated DC voltage control backend [11, 14]. [3] also supports dual-band operation, but focuses on blocking the signal from one band (either 2.4 GHz or 5 GHz) from penetrating through, whose purpose is entirely different from RF-Bouncer. The most relevant work is [31], which proposes a similar structure to support dual-band frequencies of the same polarization, but it only focuses on simulation and merely fabricates two meta-atoms as a proof-of-concept prototype. Compared with the existing dual-band design, RF-Bouncer leverages PIN diodes and a simple square patch to achieve a programmable dual-band metasurface that supports dual-band operation with the same polarization. Due to the simplicity of its structure, the proposed metasurface is easy to fabricate and thus can be easily embedded into the environment to support various IoT devices. Furthermore, RF-Bouncer designs a dual-band beam-forming algorithm that can quickly configure the states of all meta-atoms to accurately steer the incident signal towards the desired departure angle, which has not been implemented by any of the prior works.

### 3 Hardware Design of the Metasurface

In this section, We introduce the design of the meta-atom followed by a description of the overall architecture of the whole metasurface.

#### 3.1 Design Goal and Challenges

**Design goals.** To support diverse IoT devices in complex indoor environments, we have the following two design goals

for RF-Bouncer’s metasurface:

*Goal 1: Concurrent dual-band communication.* The metasurface must support concurrent wireless communication over two widely separated frequency bands, *e.g.*, 2.4 GHz and 5 GHz in our current implementation.

*Goal 2: Dual-band programmability.* The metasurface should have dual-band programmability to facilitate concurrent beam-forming for communication at two frequency bands.

**Design challenges.** To achieve of design goals, we also face the following design challenges:

*Challenge 1: Discrepancy in electric length.* To maximize the communication efficiency, the electric length (physical size) of the meta-atoms depends on the operating frequency, *i.e.*, the electric length should be half of the signal wavelength. There exists a large discrepancy in the electric length of two widely separated bands, for example, the electric length is 6 cm and 3 cm for signals at frequency 2.4 GHz and 5 GHz, respectively. Therefore, it is difficult to fabricate hardware with a fixed physical dimension but multiple resonance frequencies.

*Challenge 2: Enabling programmability.* Empowering the meta-atoms with programmability without affecting the reflection efficiency is the second challenge.

### 3.2 Design of Meta-Atoms

In this section, we first introduce the hardware architecture of the meta-atoms followed by the description of the programmability of meta-atoms.

#### 3.2.1 Dual-band Meta-Atoms

**The basic structure.** We propose to build our meta-atom based on the *metal-backed patch square structure*, which consists of three tightly connected layers: a metallic square patch on the top, a dielectric cuboid in the middle, and a metallic sheet at the bottom, just as shown in Figure 2. According to the cavity model theory [19], the resonant frequency of such a patch structure is given as:

$$f = \frac{c}{2\sqrt{\epsilon_{re}}} \cdot \frac{1}{l_e} \quad (1)$$

where  $c$  is the free-space speed of light. The parameter  $\epsilon_{re}$  is effective dielectric constant of the dielectric cuboid, which is

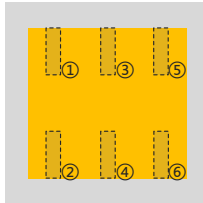


Figure 4: Different locations of slots in the meta-atom.

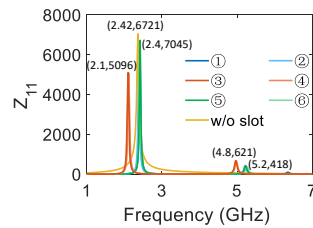


Figure 5: Surface impedance under different single slots.

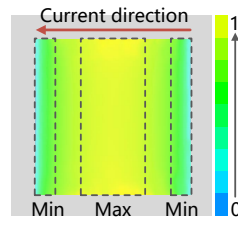


Figure 6: Current distribution of the incipient patch.

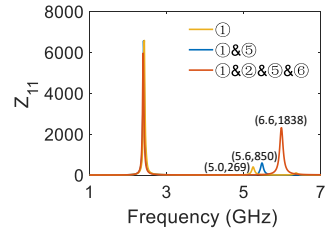


Figure 7: Surface impedance with different number of slots.

given as:

$$\epsilon_{re} = \frac{\epsilon_r + 1}{2} + \frac{\epsilon_r - 1}{2} \left( 1 + \frac{12h}{w} \right)^{-\frac{1}{2}} \quad (2)$$

where  $\epsilon_r$  is the fundamental dielectric constant of the material that makes up the dielectric cuboid,  $w$  is the width of the patch, and  $h$  is the height of the dielectric cuboid. The parameter  $l_e$  is the effective length of the patch, which is given as:

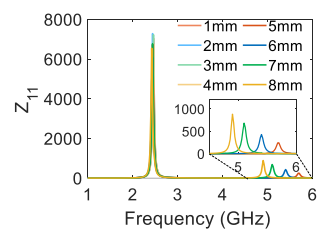
$$l_e = l + 0.824h \cdot \frac{(\epsilon_{re} + 0.3)(\frac{w}{h} + 0.264)}{(\epsilon_{re} - 0.258)(\frac{w}{h} + 0.8)} \quad (3)$$

where  $l$  is the length of the patch. We know from Eqn. 1, 2, and 3 that the resonate frequency of the structure is determined by the length  $l$ , the width  $w$  of the patch, and the height  $h$  of the dielectric cuboid.

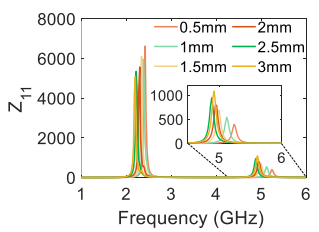
To embed more meta-atoms within one metasurface, we prefer area-efficient design, *i.e.*, smaller width  $w$  and length  $l$ . We leverage High Frequency Structure Simulator (HFSS) to conduct comprehensive simulations to quantitatively examine the relationship between the resonant frequency and the physical dimension of the meta-atoms. From the result in Figure 3 (a), we observe that, for a fixed dielectric cuboid height  $h$ , decreasing the  $w$  and  $l$  results in increased resonant frequency. Therefore, to maintain the resonant frequency at 2.4 GHz, an area-efficient meta-atom inevitably leads to a thick dielectric cuboid. To balance the size of meta-atom and thickness of the metasurfaces, we conduct extensive off-line simulations and chose the combination of  $w = 17.5\text{mm}$ ,  $l = 17.5\text{mm}$  and  $h = 6.8\text{mm}$  for our meta-atom. The final result is illustrated in Figure 3 (b), from which we see that the resonance frequency is indeed at 2.4 GHz.

**Dual-band operation.** To empower the meta-atom with a dual-band capability, we propose to fine-tune the metal-backed patch square structure to generate a second resonant frequency at 5 GHz while keeping the first resonant frequency at 2.4 GHz. Inspired by the theory of slot antenna [5], we propose to etch slots on the patch to generate additional resonant frequency, since the slots on the patch would change the path of the stimulated current and thus the resonant frequency. The final patch structure and thus the resonant frequency depends on the location and the number of slots we etch to the patch.

To study the relationship between the location of the slot and the resonant frequency, we pick six candidate slot positions on the patch, as shown in Figure 4 and leverage HFSS



(a) The length of slot.



(b) The width of slot.

Figure 8: The impact of different slot lengths and widths.

simulation to calculate the resonant frequency. We plot the simulation results in Figure 5, from which we observe that the slots located at the edge of the patch, *i.e.*, the slots ①, ②, ⑤, and ⑥, have minimum impact on the first resonant frequency, but indeed generate the second resonant frequency. The slots at the center, *i.e.*, the slots ③ and ④, however, significantly change the first resonant frequency (shifting it from 2.4 GHz to 2.1 GHz). To explain the rational behind such a phenomenon, we plot the current distribution of the original frequency (2.4 GHz) is shown in Figure 6. We see that the distribution is highly unbalanced: the current at the edge is much weaker than the current at the center of the patch. According to [21], narrow slots located close to the current minima have a minor perturbation to the original resonant frequency. Consequently, we should etch the slots at the edge of the patch to maintain the first resonant frequency at 2.4 GHz.

Even though a new resonant frequency is successfully excited, the reflected signal by the meta-atom is weak at the new resonant frequency, since the impedance between the meta-atom and the free space is close to each other. Specifically, the reflection coefficient  $\Gamma$  of an antenna measures the portion of re-radiated signal, whose value is given as  $\Gamma = \frac{Z_{11} - Z_0}{Z_{11} + Z_0}$ , where  $Z_0 = 120\pi\Omega$  is the impedance of free space. We can see that a larger difference between  $Z_{11}$  and  $Z_0$  means more power of the incident signal re-radiates. To obtain more energy from reflective signal, we propose to increase the surface impedance and thus increase the impedance difference between  $Z_{11}$  and  $Z_0$ . Our solution is to etch multiple slots at locations with small current to form an antenna array. Figure 7 depicts the  $Z_{11}$  of the meta-atom, with the number of etched slots varying from one to four. We see that the surface impedance indeed increases with the number of slot increases, but the second resonance frequency also diverges from the desired 5 GHz.

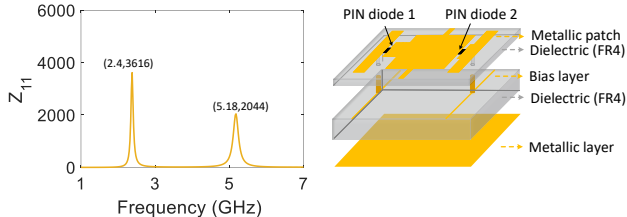


Figure 9: Surface impedance of final slot size.

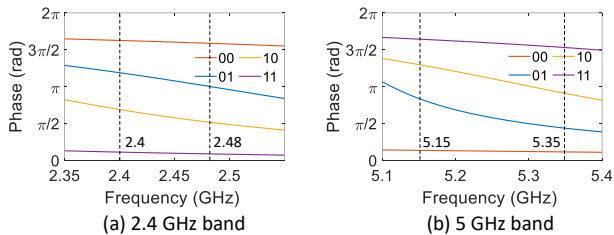


Figure 11: Reflection phase of different frequency bands.

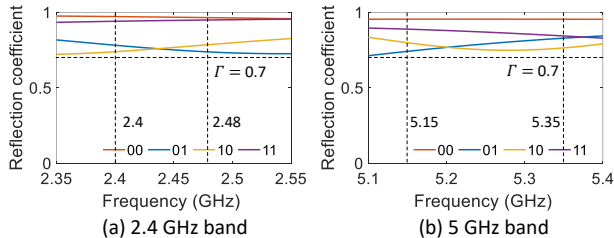


Figure 12: Reflection coefficient of 2.4 GHz and 5 GHz.

We, therefore, further fine-tune the physical dimensions of the slots to shift the second resonant frequency back to 5 GHz. We use HFSS to calculate the impedance of the meta-atom with varying slot length  $l_s$  and width  $w_s$ , and plot the results in Figure 8. We see that the increase of both  $l_s$  and  $w_s$  leads to a decrease in second resonant frequency. We choose the combination of  $l_s = 7\text{mm}$  and  $w_s = 0.5\text{mm}$  as our final solution. The final impedance of the meta-atom is plotted in Figure 9, from which we see that our optimized meta-atom not only shifts the resonant frequency back but also maximizes the reflection efficiency at two operating frequency bands.

### 3.2.2 Empowering Programmability for Meta-Atoms

To empower the meta-atom with phase-shifting capability, our basic solution is to embed tunable electronic components into the metallic patch. By programming the state of the electronic components, we change the surface impedance of meta-atom and thus the introduced phase shifts. Specifically, we select PIN diodes as our basic tunable electronic component. We select PIN diodes over varactors because PIN diode only requires two different DC voltage levels rather than precise and continuous voltage values, significantly reducing the design complexity and insertion loss [14]. We etch a rectangle slot under “U” slots and embed two PIN diodes into each slot, just as shown in Figure 10 (Please refer to Appendix A for the detailed design). By controlling the DC voltage, we obtain four

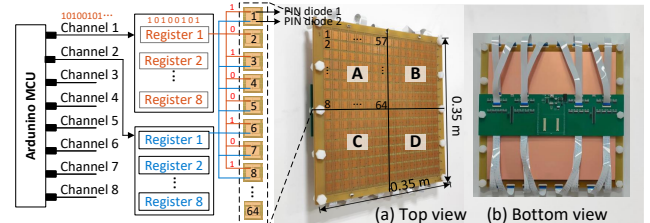


Figure 13: The control architecture of the RF-Bouncer.

stages for each meta-atom, resulting in four phase shifts. We employ HFSS to simulate the phase and reflection coefficient of each stage, and plot the results in Figure 11. We see that the phase difference between each state is about  $\pi/2$  at 2.4 GHz and 5 GHz frequency bands. In addition, from Figure 12, we find that the reflection coefficient is stably higher than 0.7 in each stage at two separated frequency bands, implying each state has small impact on the power of the reflective signal. Thus, we can use the final meta-atom as a 2-bit phase shifter.

### 3.3 Metasurface by Assembling Meta-Atoms

RF-Bouncer’s metasurface is designed by assembling multiple optimized meta-atoms. We build a prototype of RF-Bouncer’s metasurface that consists of  $16 \times 16$  meta-atoms. All the meta-atoms are evenly distributed inside an area of  $0.35 \times 0.35\text{m}^2$ , with a distance of  $19.5\text{mm}$  between adjacent meta-atoms, as shown in Figure 13. To reconfigure the PIN diode states of each meta-atom, we embed a bias layer to transmit DC bias voltage to each PIN diode (SMP1340-040LF PIN diodes [1]).

**The controller.** To configure the whole metasurface, we design a control circuit module consisting of an Arduino DUE controller and 64 SN74LV595 shift registers to provide different DC voltages (0 V or 5 V) for each meta-atom. Specifically, we divide the entire MTS board into 4 zones, as shown in Figure 13. For each zone, we use two channels in the Arduino MCU to transmit a data stream with 128 bits to control 128 PIN diodes. Due to limited GPIO pins, each channel connects 8 registers to store 64 bits. Once the enabled port is triggered, each register transmits 8 different DC voltages to respectively control 8 PIN diodes in each meta-atom. Via the above set up, the controller is now able to independently configure the state of each meta-atom’s PIN diode. In our system, RF-Bouncer’s power consumption is only at the level of mW since the metasurface itself does not emit any power.

## 4 Beamforming Through RF-Bouncer

### 4.1 Problem Formulation

RF-Bouncer supports dual-band beamforming in 3-D space. Given the angle  $\theta_i = (\alpha_i, \beta_i)$  of the incident signal, by applying appropriate phase shift  $\gamma_{m,n}$  on a matrix of  $M \times N$

meta-atoms, RF-Bouncer's metasurface beamforms the incident signal towards arbitrary angle  $\theta_d = (\alpha_d, \beta_d)$  in the 3-D space, where  $\alpha$  and  $\beta$  represent the azimuth and elevation angle, respectively, just as shown in Figure 14. RF-Bouncer has the following two working modes:

**Single-band mode.** In this mode, RF-Bouncer focuses on finding the phase shift  $\gamma_{m,n}$  of every meta-atom that enables the metasurface beamforming the incident signal at a single frequency band (either 2.4 GHz or 5 GHz) towards an arbitrary angle in 3-D space. RF-Bouncer works in this mode when there only exists wireless communication over a single frequency band.

**Dual-band mode.** In this mode, RF-Bouncer must finds the optimal phase shift  $\gamma_{m,n}$  for every meta-atom so that the metasurface simultaneously beamforms the wireless signals at 2.4 GHz and 5 GHz with incident angle  $\theta_i^{2.4G}$  and  $\theta_i^{5G}$ , towards the departure angle of  $\theta_d^{2.4G}$  and  $\theta_d^{5G}$ , respectively. RF-Bouncer works in this mode if there exist concurrent dual-band transmissions.

## 4.2 Single Band Beamforming

For the purpose of illustration, we begin the introduction of RF-Bouncer's single-band beamforming algorithm with a simple case where we beamforming in 2-D space using a metasurface consists of two meta-atoms. We then generalize the algorithm to beamforming in 3-D space with a metasurface consisting of a matrix of  $M \times N$  equally spaced meta-atoms.

**A two-element linear array in 2-D space.** We use the example of a two-element linear array to illustrate our beamforming algorithm. As shown in Figure 15 (a), the signal travels different distances before reaching two meta-atoms of the array, resulting in phase differences. Supposing the phase of signal received by the first meta-atom is 0, then the phase vector induced by the incident path is given as:

$$\phi^I(\theta_i, f_c) = \frac{2\pi f_c}{c} \cdot d \begin{bmatrix} 0 \\ \cos \theta_i \end{bmatrix} \quad (4)$$

where  $f_c$  is the central frequency of the wireless signal and  $d$  is the distance between two meta-atoms. Similarly, the signal departure also results in phase difference. The phase vector induced by the departure path is given as:

$$\phi^T(\theta_d, f_c) = \frac{2\pi f_c}{c} \cdot d \begin{bmatrix} \cos(\pi - \theta_d) \\ 0 \end{bmatrix} \quad (5)$$

The meta-atoms shift the signal by  $\gamma = [\gamma_1, \gamma_2]^T$  before reflecting the signal, just as shown in Figure 15 (b). Therefore, the phase of the signals reflected by two meta-atoms along the wavefront at the departure angle  $\theta_d$  is given as:

$$\phi(\theta_i, \theta_d, f_c, \gamma) = \phi^I + \gamma + \phi^T = \frac{2\pi f_c}{c} \cdot d \begin{bmatrix} \cos(\pi - \theta_d) \\ \cos \theta_i \end{bmatrix} + \begin{bmatrix} \gamma_1 \\ \gamma_2 \end{bmatrix} \quad (6)$$

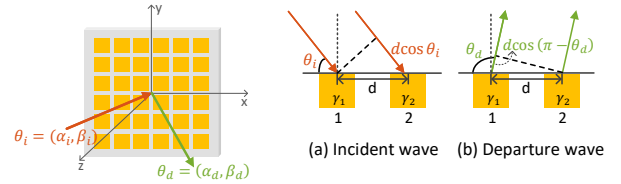


Figure 14: A metasurface in 3D space. (a) Incident wave (b) Departure wave

Figure 15: A linear array in 2D space.

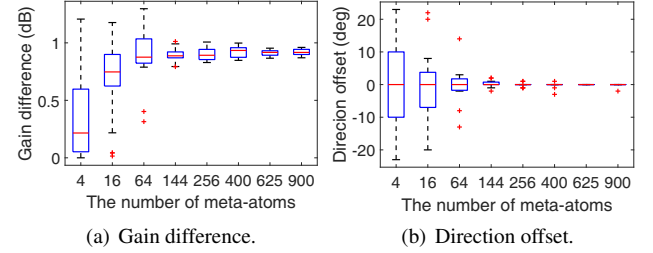


Figure 16: Beamforming gain difference and direction offset between the continuous solution  $\gamma_{m,n}$  and the discrete solution  $Q_{2-bit}(\gamma_{m,n})$  after quantization.

Beamforming the signal towards departure angle  $\theta_d$  requires signals adding constructively, *i.e.*, the phase of signal reflected by all the meta-atoms must be the same. In the above two-element case, the phase shifts  $\gamma$  applied to two meta-atoms should satisfy the following equation:

$$\gamma_2 - \gamma_1 = \frac{2\pi f_c}{c} \cdot d (\cos(\pi - \theta_d) - \cos \theta_i) \quad (7)$$

If we set the phase shift of the first meta-atom to zero, *i.e.*,  $\gamma_1 = 0$ , the phase shift of the second meta-atom can be directly calculated according to the above equation.

**Generalization.** We now generalize the above beamforming algorithm to a metasurface embedded with a matrix of  $M \times N$  meta-atoms in 3-D space. The phase vector of the incident path in 3-D space becomes:

$$\phi^I(\theta_i, f_c) = \frac{2\pi f_c}{c} \cdot d \begin{bmatrix} 0 & \dots & (N-1)v_i \\ \dots & \dots & \dots \\ (M-1)u_i & \dots & (M-1)u_i + (N-1)v_i \end{bmatrix} \quad (8)$$

where  $u_i = \cos \alpha_i \sin \beta_i$  and  $v_i = \sin \alpha_i \sin \beta_i$ . Similarly, the phase vector of the departure path is given as

$$\phi^T(\theta_d, f_c) = \frac{2\pi f_c}{c} \cdot d \begin{bmatrix} (M-1)u_d + (N-1)v_d & \dots & (N-1)v_d \\ \dots & \dots & \dots \\ 0 & \dots & (M-1)u_d \end{bmatrix} \quad (9)$$

where  $u_d = \cos \alpha_d \sin \beta_d$  and  $v_d = \sin \alpha_d \sin \beta_d$ . Combing Eqn 8 and 9 with Eqn 6, we have enough equations to derive the phase shifts  $\gamma_{m,n}$  that we should apply to each meta-atom of the metasurface.

**Discrete phase shifts of meta-atoms.** The optimal phase shift  $\gamma_{m,n}$  we calculate according to above section is continuous. Recall that each meta-atom in the metasurface is essentially a 2-bit phase shifter that only provides four possible phase

shifts:  $0$ ,  $\frac{\pi}{2}$ ,  $\pi$  and  $\frac{3\pi}{2}$ . We apply the following quantization rule to find the discrete solution of phase shifts  $\gamma_{m,n}$ :

$$Q_{2\text{-bit}}(\gamma_{m,n}) = \begin{cases} 0, & \text{otherwise} \\ \pi/2, & \text{if } \pi/4 \leq \gamma_{m,n} < 3\pi/4 \\ \pi, & \text{if } 3\pi/4 \leq \gamma_{m,n} < 5\pi/4 \\ 3\pi/2, & \text{if } 5\pi/4 \leq \gamma_{m,n} < 7\pi/4 \end{cases} \quad (10)$$

Phase quantization brings phase error and inevitably degrades the beamforming performance. To quantitatively investigate the impact of phase quantization, we traverse all the possible combinations of incident angle  $\theta_i$  and departure angle  $\theta_d$  and calculate one continuous solution  $\gamma_{m,n}$  and one discrete solution  $Q_{2\text{-bit}}(\gamma_{m,n})$  for each combination  $(\theta_i, \theta_d)$ . We calculate the gap of the beamforming gain and beamforming direction between the continuous solution and the discrete solution and plot the results in Figure 16. We clearly see that with the number of meta-atoms in the metasurface increases, the gap of beamforming gain stabilizes at 1 dB, while the direction offset decreases and eventually gets very close to zero. This result is in line with the prior work [35]. RF-Bouncer's metasurface has  $16 \times 16 = 256$  meta-atoms so the degradation of the beamforming performance becomes negligible.

### 4.3 Dual-band Beamforming

**Challenge.** For single band beamforming, we are able to calculate the optimal phase shifts  $\hat{\gamma}_{m,n}$  of every meta-atom that strictly meeting the requirement of the beamforming: the signal reflected by all meta-atom has exact the same phase so they superimpose constructively at the receiver. Ideally, if each meta-atom is able to compensate the signal with two arbitrary phase shifts at two operating frequency band, then a naive solution would be separately finding the optimal phase shifts for two frequency band, *i.e.*,  $\hat{\gamma}_{m,n}^{2.4G}$  for 2.4 GHz band and  $\hat{\gamma}_{m,n}^{5G}$  for 5 GHz band, and then applying the optimal phase shifts to each meta-atom. Our meta-atom, however, only has 2-bit programmability (four states) and thus provides four fixed combination of phase shifts at two frequency band. Specifically, for each state  $\eta_{m,n}$ , the phase shifts at two frequency band can be derived via a known mapping:

$$\begin{aligned} \gamma_{m,n}^{2.4G} &= P_{2.4G}(\eta_{m,n}) \\ \gamma_{m,n}^{5G} &= P_{5G}(\eta_{m,n}) \end{aligned} \quad (11)$$

We list the mapping between the state of meta-atom and the phase shifts introduced by the meta-atom at that state at both 2.4 GHz and 5 GHz band in Table 1.

Due to each meta-atom's limited phase combinations at two frequency bands, it is impossible to simultaneously implement the optimal phase shifts  $\hat{\gamma}_{m,n}^{2.4G}$  and  $\hat{\gamma}_{m,n}^{5G}$  on our metasurface. Consequently, it is also impossible to find analytical solutions that strictly meet the phase requirement of the beamforming. Instead, we turn to search for the optimal combination of

$\eta_{m,n}$	$P_{2.4G}$	$P_{5G}$	$\parallel$	$\eta_{m,n}$	$P_{2.4G}$	$P_{5G}$
00	$3\pi/2$	0		10	$\pi/2$	$\pi$
01	$\pi$	$\pi/2$		11	0	$3\pi/2$

Table 1: The mapping between the state of meta-atom and the phases shift the meta-atom at that state introduces to signals with central frequency of 2.4 GHz and 5 GHz.

states  $\eta_{m,n}$  of meta-atom that maximize the total gain of the main lobes of the metasurface's beamforming patterns at two frequency bands.

**Dual-band link optimization.** Given the incident angle  $\theta_i^{2.4G}$ , the strength of the 2.4 GHz signal reflected by the metasurface along the departure angle  $\theta_d^{2.4G}$  is given as:

$$\begin{aligned} S_{2.4G}(\theta_i^{2.4G}, \theta_d^{2.4G}, \eta) &= a_{2.4G}(\theta_d^{2.4G}) \sum_{1}^M \sum_{1}^N e^{j\phi(\theta_i^{2.4G}, \theta_d^{2.4G}, f_{2.4G}, \eta)} \\ &= a_{2.4G}(\theta_d^{2.4G}) \sum_{1}^M \sum_{1}^N e^{j\phi(\theta_i^{2.4G}, \theta_d^{2.4G}, f_{2.4G}, P_{2.4G}(\eta_{m,n}))} \end{aligned} \quad (12)$$

where  $a_{2.4G}(\theta_d^{2.4G})$  represents the amplitude of 2.4 GHz signal reflected by each meta-atom along direction  $\theta_d^{2.4G}$ , whose value is identical across all identical meta-atoms. Similarly, the strength of 5 GHz signal reflected by the metasurface can be represented as:

$$S_{5G}(\theta_i^{5G}, \theta_d^{5G}, \eta) = a_{5G}(\theta_d^{5G}) \sum_{1}^M \sum_{1}^N e^{j\phi(\theta_i^{5G}, \theta_d^{5G}, f_{5G}, P_{5G}(\eta_{m,n}))}. \quad (13)$$

Our goal is to search for the optimal meta-atom states  $\eta^*$  that maximizes the total signal strength along direction  $\theta_d^{2.4G}$  and  $\theta_d^{5G}$ , given incident signal angle  $\theta_i^{2.4G}$  and  $\theta_i^{5G}$ :

$$\eta^* = \arg \max_{\eta} \left( |S_{2.4G}(\theta_i^{2.4G}, \theta_d^{2.4G}, \eta)| + |S_{5G}(\theta_i^{5G}, \theta_d^{5G}, \eta)| \right). \quad (14)$$

To prevent over-optimizing single band and thus guarantee the fairness between two bands, we further adjust our objective function to:

$$\eta^* = \arg \min_{\eta} \left( \left( |S_{2.4G}^*| - |S_{2.4G}(\theta_i^{2.4G}, \theta_d^{2.4G}, \eta)| \right) + \left( |S_{5G}^*| - |S_{5G}(\theta_i^{5G}, \theta_d^{5G}, \eta)| \right) \right) \quad (15)$$

where  $S_{2.4G}^*$  and  $S_{5G}^*$  are the theoretical maximum signal strength achieved when we single-band beamform on 2.4 GHz and 5 GHz band using continuous phase shifter, respectively. We employ genetic algorithm (GA) algorithm [33] to solve our optimization problem described in Eqn 15. To speed up the search, instead of generating a random initial population, we use the coding patterns optimized for each single frequency band as a set of initial chromosomes in the initial population of the GA algorithm.

We conduct an experiment to verify the effectiveness of the proposed dual-band links optimization algorithm. In this

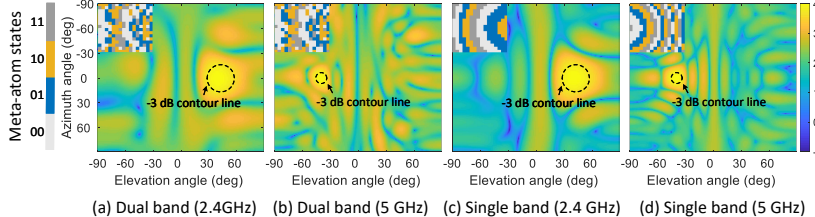


Figure 17: The beam patterns of single-band links and dual-band links, respectively.

experiment, we set the incident angle of 2.4 GHz and 5 GHz signal to  $(\alpha_i^{2.4G} = 0^\circ, \beta_i^{2.4G} = 0^\circ)$  and  $(\alpha_i^{5G} = 0^\circ, \beta_i^{5G} = 0^\circ)$ , respectively. The desired beamforming direction of 2.4 GHz and 5 GHz signal are set to  $(\alpha_d^{2.4G} = 0^\circ, \beta_d^{2.4G} = 40^\circ)$  and  $(\alpha_d^{5G} = 0^\circ, \beta_d^{5G} = -40^\circ)$ , respectively. After applying the optimal state  $\eta_{m,n}^*$  to each meta-atom, the beam pattern of the whole metasurface is plotted in Figure 17, from which we could see that: 1) the two mainlobes obtained by dual-band beamforming well match the desired angles; 2) the sidelobe levels are much lower than the mainlobe levels. In addition, the mainlobe beamwidth of the 2.4 GHz band is wider than the 5 GHz band. The reason is that the size of the meta-atom is more suitable for 5 GHz band, but this issue can be easily solved by increasing the number of meta-atoms to generate a narrow beam of mainlobe [38]. 3) dual-band beamforming has a lower gain about 3 dB than single-band beamforming, while the -3 dB beamwidth is only slightly wider than single-band beamforming (Figure 17 (c) and (d)).

#### 4.4 Harnessing the Ambient Multipath

We observe that there exists some meta-atoms that contribute negligible power or even have negative impact on the main lobe, but significantly affect the distribution of the side lobes, especially when the metasurface is configured for dual-band operation. To demonstrate such a phenomenon, we change the states of a small group of meta-atoms in Figure 17 (a) and (b), and plot the 3-D beam patterns of the new metasurface configuration in Figure 18. Comparing the beam patterns in these two figures, we see that the direction and gain of main lobes still retain, but the side lobes change dramatically. The signal of the side lobes does not travel directly towards the receiver, but may still reach the receiver after being reflected by diverse objects in the propagation environment. We propose to further improve the signal strength by adjusting the pattern of side lobes of the metasurface.

The key challenge we face is to select the group of meta-atoms that mainly affects the side lobes. Since the target meta-atoms have negligible or even negative impact on the main lobe, the phase of the signal reflected by the target meta-atoms must be misaligned (difference larger than  $\pi/2$ ) with the phase of the main lobes. Without loss of generality, we denote the desired beamforming directions at 2.4 GHz and 5 GHz bands are  $(\alpha_{2.4G}, \beta_{2.4G})$  and  $(\alpha_{5G}, \beta_{5G})$ , respectively.

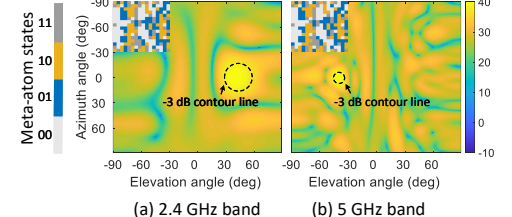


Figure 18: The beam patterns when changing negative meta-atoms.

Then, the phase of mainlobe is given as:

$$PM_{2.4G} = \angle \sum_{m=1}^M \sum_{n=1}^N e^{j\phi(\theta_i^{2.4G}, \theta_d^{2.4G}, f_{2.4G}, P_{2.4G}(\eta_{m,n}^*))} \quad (16)$$

$$PM_{5G} = \angle \sum_{m=1}^M \sum_{n=1}^N e^{j\phi(\theta_i^{5G}, \theta_d^{5G}, f_{5G}, P_{5G}(\eta_{m,n}^*))} \quad (17)$$

where  $\eta_{m,n}^*$  is the optimal states of meta-atoms we calculated according to Eqn 15. Then, we find separate sets of target meta-atoms at two frequency bands, respectively:

$$TU_{2.4G} = \left\{ \{m,n\} \mid |PM_{2.4G} - \phi(\theta_i^{2.4G}, \theta_d^{2.4G}, f_{2.4G}, \eta_{m,n})| \geq \frac{\pi}{2} \right\}, \quad (18)$$

$$TU_{5G} = \left\{ \{m,n\} \mid |PM_{5G} - \phi(\theta_i^{5G}, \theta_d^{5G}, f_{5G}, \eta_{m,n})| \geq \frac{\pi}{2} \right\}, \quad (19)$$

where  $m$  and  $n$  vary from 1 to 16 in our system. Finally, we select the intersection of two sets of target meta-atoms as the final solution:

$$TU = TU_{2.4} \cap TU_{5G}. \quad (20)$$

The intersection  $TU$  includes meta-atoms that have negligible or even negative impact for 2.4 GHz and 5 GHz band simultaneously, so we are safe to change the states of the meta-atoms in  $TU$  to adjust the side lobes while at the same time guarantees minimum impact on main lobes of two band. We iterate all possible combinations of state and choose the one that provides best signal quality. It is worth noting that when the number of variable meta-atoms is large, it could take a long time for exhaustive search. To reduce the search time, one potential solution is to divide the whole metasurface into several parts. For each part, the variable meta-atoms change their state in the same way. Therefore, the number of exhaustive search will be reduced to a small number. For example, we divide the whole metasurface into 4 parts. Therefore, all possible combinations of state will be reduced to 512 (i.e.,  $4^4$ ). Assuming Wi-Fi packets are collected at a rate of 1,000 packets per second, the search time will be 0.5 seconds.

#### 4.5 Beam Alignment

To accurately beam the reflected signal towards the receiver, we need to know the signal incident angle  $\theta_i$  and departure

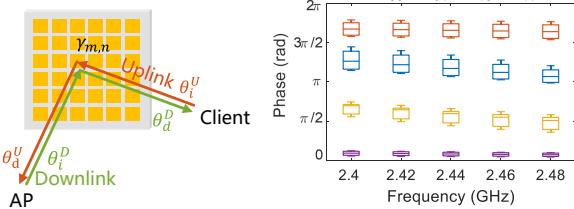


Figure 19: Illustration of uplink and downlink. Figure 20: Phase offset under different incident angles.

angle  $\theta_d$ . We observe that in a typical Wi-Fi system, the access point is static for most of the cases. Therefore, the signal incident and departure angle is fixed and known for downlink and uplink Wi-Fi communication, respectively (Figure 19). We propose to search for the unknown angle, *i.e.*, incident angle for uplink and departure angle for downlink.

**Beam search for downlink.** For downlink communication, we need to search for the departure angle  $\theta_d$ . In  $n$ -th round of beam search, the metasurface configures its meta-atoms to point the main lobe towards a specific angle  $\theta_d^n$ . After receiving one packet under such a configuration, the receiver embeds one bit inside its ACK to inform the metasurface whether the received signal quality has increased or not comparing with the previous configuration, *i.e.*, bit 1 represents increase and bit 0 means decrease. We equip the metasurface with a Wi-Fi receiver to overhear the ACK. After iterating all possible departure angles, we select the  $\theta_d$  that provides the highest received signal quality as our results.

To speed up the searching process, we implement a two-stage searching algorithm. In the first stage, we search with a relatively large step size of  $20^\circ$ . After obtaining the rough direction, we then search with a small step size of  $5^\circ$  to fine-tune the results. A step size of  $5^\circ$  is fine-grain enough since the beamforming gain only decreases less than 1 dB at directions that are  $2.5^\circ$  apart from the beamforming direction, according to both our simulation and empirical results.

**Bidirectional communication.** We observe that, due to reciprocity, we only need to perform beam search in one direction. First, according to *channel reciprocity*, the phase shifts that should be applied to each meta-atom for beamforming is the same even when we swap the value of the incident angle  $\theta_i$  and departure angle  $\theta_d$ . As shown in Figure 19, the signal travels exactly the same distance no matter the AP or the client is the sender, introducing the same amount of phase variations. Therefore, the phase shifts required to meet the phase requirement of beamforming is also the same.

Second, the optimized meta-atom introduces the same amount of phase shifts to the signal, regardless of the signal incident angle. To verify that, we use HFSS to calculate the phase shifts introduced by meta-atom by varying the incident angle, operating frequency and state of meta-atom. We plot the distribution of phase shifts in Figure 20, from which we see that the phase variations introduced by the meta-atom is stable. According to the above analysis, the configuration

of the metasurface used for beamforming in one direction also works in the opposite direction. Such an observation significantly accelerates convergence of the beam alignment algorithm, especially when the client moves.

## 5 Evaluation

**Experimental setup.** For controlled experiments, we use USRP N210 software-defined radios with a UBX-40 daughterboard as the radio transmitter (Tx) and receiver (Rx). We conduct extensive experiments in three indoor environments to evaluate the performance of RF-Bouncer: a  $140 m^2$  duplex with two-bedroom, a  $160 m^2$  apartment and a spacious corridor environment with corner. In the default experimental setting, 2.44 GHz and 5.25 GHz are selected as the operating frequency of the 2.4 GHz band and 5 GHz band, respectively. The Tx is deployed in the normal direction of the metasurface.

### 5.1 Hardware Verification

**Dual-band beamforming verification.** This experiment compares beamforming results between single-band and dual-band coding patterns. We configure the metasurface using single-band coding patterns of 2.4 GHz and 5 GHz, and optimization dual-band coding patterns, respectively. The Rx moves along a semicircle (3 m radius) from  $-90^\circ$  to  $90^\circ$  with a step of  $10^\circ$ , while the Tx stays in the center. The Tx-metasurface distance sets as 0.5 m. Figure 21 demonstrates that both single-band and dual-band coding pattern can achieve effective beamforming results, but dual-band beamforming results come at the cost of slight decreases of signal strength or slight shift of the direction on the mainlobe.

**The performance of beamforming in dual-band.** To evaluate the beamforming performance of dual-band, we keep the Tx-metasurface distance sets as 0.5 m. We default  $\alpha = 0^\circ$  and only vary  $\beta$  in the following experiments. We move the Rx along a semicircle (3 m radius) from  $-90^\circ$  to  $90^\circ$  with a step of  $10^\circ$ . The results are shown in Figure 22, we can clearly see that the effective beamforming ranges of 2.4 GHz and 5 GHz are both  $[-60^\circ, 60^\circ]$ . Although the  $-3dB$  beamwidth becomes wider and beamforming gain becomes lower when the beamforming direction is towards the boundary, the correct directionality is retained. It is worth noting that the beamforming gain of  $0^\circ$  is slightly decreased since the Tx blocks the link between metasurface and Rx. In addition, the performance will be significantly dropped when the beamforming direction is over the boundary. In conclusion, the effective field-of-view (FoV) of beamforming is  $[-60^\circ, 60^\circ]$ .

**The effective incident angles.** We conduct experiments in the corridor to explore the effective range of incident angles. For the convenience of expression, we only mention  $\beta$  in the following and default  $\alpha = 0^\circ$ . To determine the range, we first vary incident angles by changing the direction of Tx from

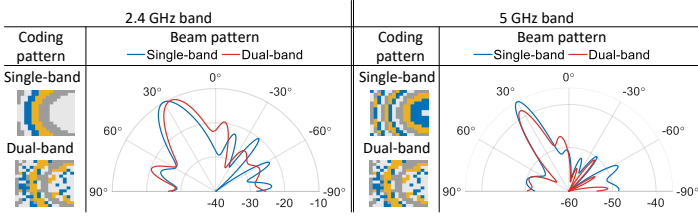


Figure 21: Results of single and dual band coding patterns.

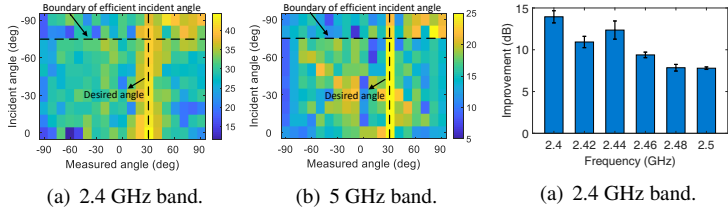


Figure 23: The performance under different incident angles.

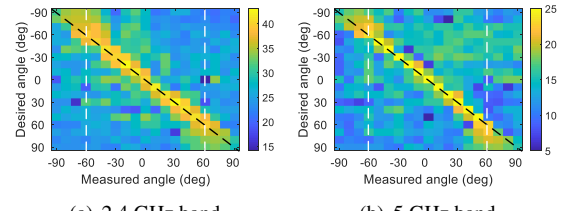


Figure 22: The results of beam steering from  $-90^\circ$  to  $90^\circ$ .

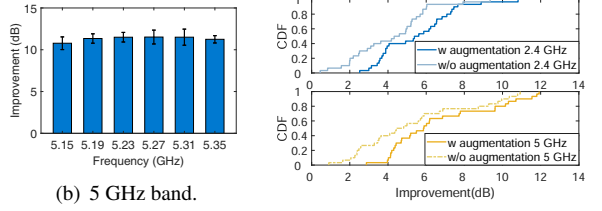


Figure 24: SNR improvement across operating frequencies.

Figure 25: Results of multipath augmentation scheme.

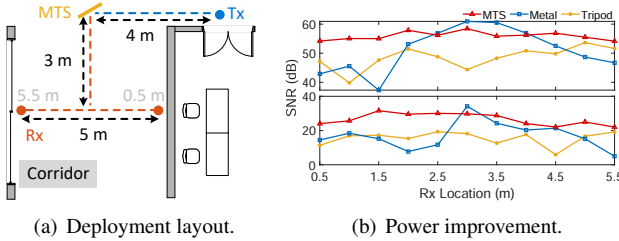


Figure 26: The performance of different reflectors.

$-90^\circ$  to  $0^\circ$  with a step of  $10^\circ$  and set the Tx-metasurface distance as 0.5 m. Then, we move Rx along a semicircle (3 m radius) from  $-90^\circ$  to  $90^\circ$  with a step of  $10^\circ$  to obtain different beam patterns under different incident angles. The desired beamforming direction is set towards  $30^\circ$ . The results are shown in Figure 23, from which we see that RF-Bouncer can achieve beamforming effectively in the desired direction when the incident angle varies from  $-70^\circ$  to  $0^\circ$ . However, the beamforming gain and direction of the mainlobe can not be guaranteed due to the incident wave being almost parallel (i.e., from  $-90^\circ$  to  $-80^\circ$ ) to the metasurface. In addition, because of the symmetry of metasurface, the same experimental results will appear in  $[0^\circ, 70^\circ]$ . To summarize, RF-Bouncer can work well as long as Tx is located in  $[-70^\circ, 70^\circ]$ .

**Performance across different spectrums.** In this experiment, we validate the performance of RF-Bouncer across different operating frequency bands. The distance of Tx-metasurface is 0.5 m, and the direction of the incident wave is perpendicular to the metasurface. The distance between Rx and metasurface is set to 3 m. The direction of the emergent wave focuses on  $(30^\circ, 0^\circ)$  and Rx is located in the same direction. One case is from 2.4 GHz to 2.5 GHz with a step of 0.02 GHz. Figure 24(a) shows the SNR can be increased by over 7.79 dB (up to 13.94 dB). Another case is from 5.15 GHz to 5.35 GHz with a step of 0.04 GHz. Figure 24(b) shows the SNR can be improved by over 10.78 dB (up to 11.5 dB). Therefore, RF-

Bouncer can be applied to ubiquitous commercial IoT devices working in 2.4 GHz and 5 GHz bands.

## 5.2 Communication Performance

**Multipath augmentation verification.** To examine the effectiveness of multipath augmentation described in Section 4.4, we conduct experiments in a representative 3D scenario (Figure 28 (a)). Specifically, we fix the location of the transmitter and randomly move the receiver to 30 locations. Then, for each location, we respectively collect the measurements with/without multipath augmentation at 2.4 GHz and 5 GHz. Figure 25 plots the CDF of signal strength improvement at two frequency bands. We can see that the median improvements with/without multipath augmentation at 2.4 GHz and 5 GHz are respectively 4.32 dB, 5.38 dB and 4.43 dB, 5.89 dB. These results demonstrate that our multipath augmentation scheme can effectively harness the ambient multipath to improve the link SNR.

**The performance of different reflectors.** By placing RF-Bouncer at a corridor intersection, the blind spot around the corner can be illuminated. We conduct an experiment in a spacious corridor environment, as shown in Figure 26(a). The metasurface is placed at the corner, receiving signals from  $(-45^\circ, 0^\circ)$ , and reflecting a fan beam from  $(-85^\circ, 0^\circ)$  to  $(5^\circ, 0^\circ)$ . The Tx is 4 m away from the metasurface; whereas Rx is 3 m away moved across a 5 m distance. Figure 26(b) compares the RSS with metasurface, a metal plane reflector with the same size as the metasurface, and the tripod without reflectors. While the metal plane creates a stronger mainlobe towards the specular direction, the RSS drastically drops as the Rx is moved to anomalous directions. In contrast, RF-Bouncer reshapes the incidental beam to cover a wider angular range and thus a larger region around the corner.

**Multi-bit beamforming verification.** The 2-bit metasurface

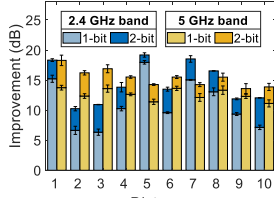
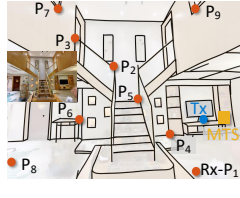
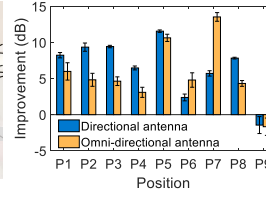


Figure 27: 1-bit V.S. 2-bit.



(a) 3D scenario Layout



(b) Power Improvement

Figure 28: Experimental results under 3D scenario.

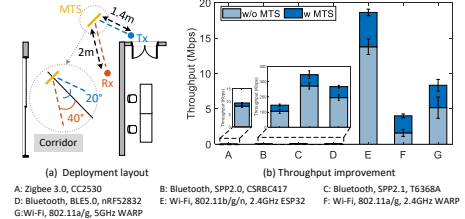


Figure 29: Experimental results of throughput improvement across different IoT devices.

respectively. Figure 28(b) shows the improvement in different channel conditions. Almost all signal strength improvements under different positions are above 2.5 dB and up to 13.5 dB. Furthermore, due to indoor multipath, the improvement of omni-directional antenna at some positions (i.e., P<sub>6</sub> and P<sub>7</sub>) in the 3D scenario is higher than directional antenna. In contrast, the improvement of P<sub>9</sub> is negative due to the following reasons: 1) the azimuth angle between P<sub>9</sub> and metasurface exceeds the effective beamforming FoV of metasurface, leading RF-Bouncer can not provide beamforming gain to it; 2) the reinforced concrete between floors blocks the LoS between Tx and Rx, causing most energy of the incident signal reflects to other directions. This issue can be easily solved by deploying multiple metasurfaces.

**Throughput across different IoT devices.** RF-Bouncer aims to enhance the signal energy of IoT devices in the NLoS scenario. Hence, in this experiment, we test IoT devices (i.e., CC2530, CSRBC417, KT6368A, nRF52832, ESP32, WARPv3) operating different frequency bands (i.e., 2.4 GHz and 5 GHz) with various protocols (i.e., Zigbee 3.0, SPP 2.0, SPP 2.1, BLE 5.0, 802.11 b/g/n, and 802.11 a/g) in a corner NLoS scenario. We use *iperf* to measure TCP throughput for ESP32 and use the WARPv3 environment for the WARPv3 boards. The NLoS deployment layout is shown in Figure 29(a). We set the Tx-metasurface distance and Rx-metasurface distance as 1.4 m and 2 m, respectively. The incident angle of metasurface is (20°, 0°) and the emerging angle is (-40°, 0°). The results with metasurface and without metasurface (referred to w MTS and w/o MTS) are shown in Figure 29(b). We can see that the minimum, median, and maximum throughput gain are 115%, 137%, and 249%, respectively. These results imply that RF-Bouncer is transparent to the working protocols and frequencies.

**SISO and MIMO links.** We now evaluate the throughput performance in SISO and MIMO communication systems. Specifically, we use two laptops equipped with AR9580 wireless cards as the transmitter and receiver, each of them has three antennas and works on the 802.11n protocol. Then, we fix the transmitter location and move the receiver to 10 locations, as shown in Figure 30(a). At each location, we respectively change the communication mode, varying from 1 × 1, 2 × 2 and 3 × 3, and use *iperf* toolbox to collect throughput measurements. Figure 30(b) shows that as the number of antennas used in communication system increases, the

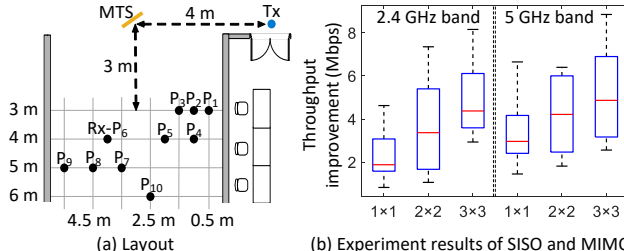
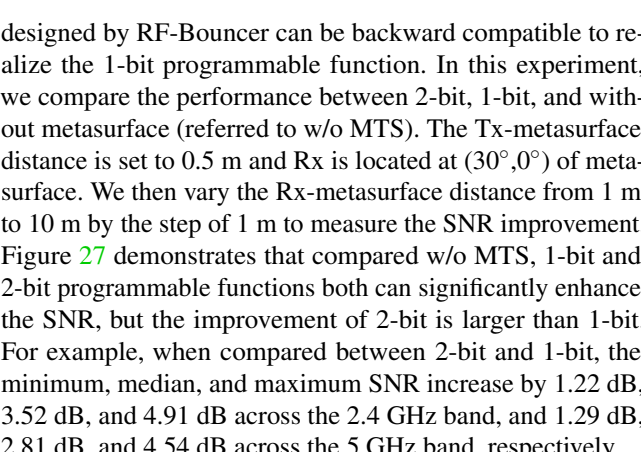


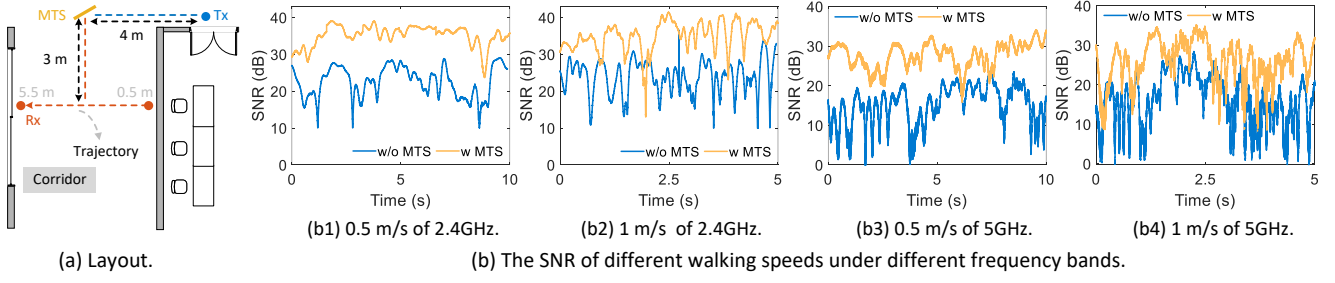
Figure 30: Throughput improvement of SISO and MIMO.

designed by RF-Bouncer can be backward compatible to realize the 1-bit programmable function. In this experiment, we compare the performance between 2-bit, 1-bit, and without metasurface (referred to w/o MTS). The Tx-metasurface distance is set to 0.5 m and Rx is located at (30°, 0°) of metasurface. We then vary the Rx-metasurface distance from 1 m to 10 m by the step of 1 m to measure the SNR improvement. Figure 27 demonstrates that compared w/o MTS, 1-bit and 2-bit programmable functions both can significantly enhance the SNR, but the improvement of 2-bit is larger than 1-bit. For example, when compared between 2-bit and 1-bit, the minimum, median, and maximum SNR increase by 1.22 dB, 3.52 dB, and 4.91 dB across the 2.4 GHz band, and 1.29 dB, 2.81 dB, and 4.54 dB across the 5 GHz band, respectively.

**Performance under 3D scenario.** We test the SNR improvement achieved by RF-Bouncer in a representative 140 m<sup>2</sup> 3D scenario (Figure 28(a)). Due to the deployment limitation, we mount the Tx and metasurface on tripods and place them at the same height up the ground. The distance of Tx-metasurface is 0.5 m. Both Rx and Tx work in the 5 GHz band. The Rx is located at 9 different locations. The height of the Rx from the ground varies from 10 cm to 5 m. The elevation angle of Rx varies from -30° to 30° and the azimuth angle of Rx varies from -30° to 40°. We measure the SNR improvement by using directional and omnidirectional antenna,

Figure 31: Performance under concurrent transmissions.

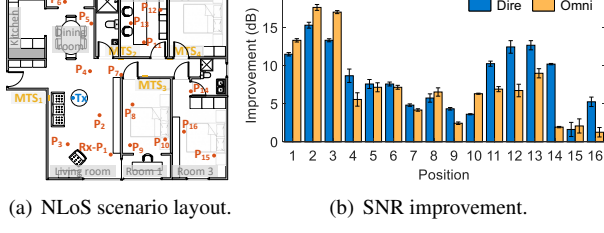




(a) Layout.

(b) The SNR of different walking speeds under different frequency bands.

Figure 32: Experimental results of different walking speeds under different frequency bands.



(a) NLoS scenario layout.

(b) SNR improvement.

throughput improvement increases in both frequency bands. For example, RF-Bouncer can achieve a median throughput improvement of 1.88Mbps, 3.37Mbps, 4.38Mbps, and 2.96Mbps, 4.22Mbps, 4.87Mbps for  $1 \times 1$ ,  $2 \times 2$  and  $3 \times 3$  at 2.4 GHz and 5 GHz, which corresponds to an improvement of up to 50% compared with the baseline in each case.

**Concurrent transmissions.** In this experiment, we evaluate RF-Bouncer’s performance in the presence of concurrent wireless links at 2.4 GHz and 5 GHz. Specifically, we fix two transmitters working at 2.4 GHz and 5 GHz in two different locations, and move two corresponding receivers to nine different location combinations. The detailed deployment is presented in Figure 31(a). In each location combination, the coding pattern of metasurface is obtained based on Sec. 4.3, and we then collect the measurements to calculate the SNR improvement when there is no metasurface. The results in Figure 31(b) shows that RF-Bouncer can simultaneously improve the SNR of two concurrent wireless links. For example, RF-Bouncer can achieve an average SNR improvement of 9.01 dB and 12.08 dB for 2.4 GHz and 5 GHz, respectively. This demonstrates that RF-Bouncer can work well for dual-band concurrent wireless transmissions.

### 5.3 Performance under Mobility

In this section, we examine the performance of RF-Bouncer in a mobile environment. We place the transmitter at a fixed location and move the receiver along a predefined trajectory with two constant speeds: 0.5 m/s (slow) and 1.0 m/s (normal). In each speed case, RF-Bouncer controller configures the metasurface in real time to accurately beam the reflected signal towards the receiver. The detailed sweep mechanism is referred to Sec. 4.5. Then, we collect the measurements

to calculate the SNR during the receiver’s movement. Figure 32 shows the real-time SNR measurements with/without metasurface (referred to w MTS and w/o MTS) in 2.4 GHz and 5 GHz. We can see that RF-Bouncer can consistently achieve a SNR improvement compared to the case without metasurface at both different speeds and different frequency bands. These results demonstrate that RF-Bouncer can work well in mobile environments. In addition, we can observe that the performance of RF-Bouncer in slow speed works better than high speed. This is because RF-Bouncer has more time to beam the signal towards the receiver. We thus will explore the high speed scenario of RF-Bouncer in future work.

### 5.4 Coverage Extension

**Whole-house coverage under cooperative work.** By placing multiple metasurfaces (MTSs) in the complex whole-house scenario, the signal coverage can be efficiently expanded. We conduct an experiment in a  $160 m^2$  place with four rooms (Figure 33(a)). Four MTSs are cooperating. MTSs independently control and the working range of each MTS is disjoint. We note that this experiment does not consider how to select a good MTS route in the central control end to achieve good performance. Instead, we manually selected a routing route to perform beamforming for each location. Specifically, the transmitter in this experiment is fixed at one location and four MTSs are also pre-fixed at different locations. The route starts at MTS<sub>1</sub>, goes through MTS<sub>2</sub> and MTS<sub>3</sub>, and ends at MTS<sub>4</sub>. Coverage includes the living room, the dining room, and three rooms. Note that missing areas that are not currently covered - such as the kitchen, room 4, and the bathrooms - can be easily covered by deploying more MTSs in the future. We set the Tx-MTS distance to 1 m and measure the SNR improvement in different locations. RSS from P<sub>1</sub> to P<sub>6</sub> is controlled by MTS<sub>1</sub>; from P<sub>7</sub> to P<sub>10</sub> is controlled by MTS<sub>2</sub>; from P<sub>11</sub> to P<sub>13</sub> is controlled by MTS<sub>3</sub>; and from P<sub>14</sub> to P<sub>16</sub> is controlled by MTS<sub>4</sub>. The results of using the omnidirectional/directional antenna (referred to Omni and Dire) and with/without the MTS (referred to w MTS and w/o MTS) are shown in Figure 33(b). We can clearly see that 1) the signal coverage can be efficiently expanded by leveraging multiple MTSs collaborative with each other; 2) the SNR is generally improved (above 1.26 dB and up to 17.65 dB) in NLoS envi-

ronments by the MTS, while the enhancements of different distances are different due to multipath; 3) MTS can achieve good performance even without LoS path between MTS and Rx (i.e., through the wall); 4) regardless of the antenna pattern, RF-Bouncer can improve the SNR.

**Corner coverage expansion.** In this experiment, we show how RF-Bouncer expands the wireless coverage at the corner scenario. As shown in Figure 34, we collect measurements with/without metasurface in both downlink and uplink for each location. From Figure 34, we can see that without metasurface, most locations around the corner have a lower SNR, especially for 5 GHz links, which only have an average SNR of 4.24 dB and 3.67 dB in downlink and uplink, respectively. This is because a signal of higher frequency has more severe path attenuation. In contrast, with the help of RF-Bouncer metasurface, most locations around the corner significantly improved SNR in both downlink and uplink at 2.4 GHz and 5 GHz. For example, RF-Bouncer can achieve an average SNR improvement of 10.30 dB (up to 26.16 dB) and 8.10 dB (up to 24.19 dB) for 2.4 GHz and 5 GHz downlinks, while an average SNR improvement of 8.78 dB (up to 25.27 dB) and 8.54 dB (up to 17.01 dB) for 2.4 GHz and 5 GHz uplinks. These results demonstrate that 1)RF-Bouncer can well expand the wireless coverage at the corner scenario; 2) RF-Bouncer can achieve good performance when Tx and Rx locations vary over a wide range of angles; 3) RF-Bouncer can work well for downlink and uplink simultaneously.

## 6 Discussion

**Multiple metasurfaces cooperation.** Cooperating multiple metasurfaces across rooms can effectively expand the wireless coverage, which is an interesting and challenging direction. In our current implementation, we manually calculate the configuration of each metasurface offline (which cannot guarantee the optimal performance) and send the configuration to each controller. In the future work, we will design an algorithm that can automatically configure the networked metasurfaces. In addition, current metasurface only consists of 256 meta-atoms with a size of  $0.35 \times 0.35 m^2$ , such a small aperture would lead to a wide beam at 2.4 GHz, which results in a worse coverage between different metasurfaces in the case of installing multiple metasurfaces. This is a limitation of our current version. Thus, to avoid this issue, one possible method is to design a larger aperture metasurface to generate a narrow beam of mainlobe.

**Operationg frequency.** Our current design has a bandwidth of 200 MHz (from 5.15 GHz to 5.35 GHz), which covers 17 WiFi channels at 5 GHz. Since commercial devices go all the way to 5.8 GHz of spectrum, we thus will optimize our meta-atom’s design to enlarge the effective working band to cover additional 5 GHz channels in the follow-up work.

**Unwanted interference induced by metasurface.** Deploy-

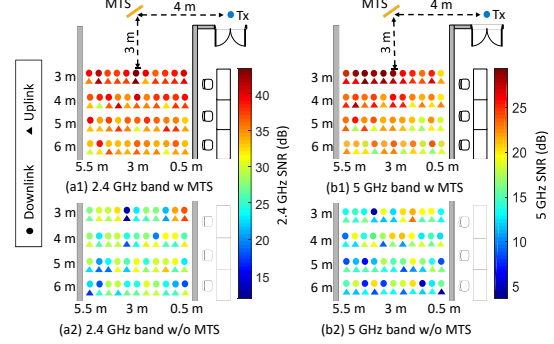


Figure 34: Corner coverage extension.

ing a smart surface to amplify some of the signals could possibly lead to interference, especially when there are multiple concurrent wireless links. But the possibility is small since the metasurface is beamforming the signal towards a specific direction, instead of omnidirectional reflection. Also, if the whole area is covered with metasurfaces, we could minimize interference by coordinating the metasurfaces.

**Practicality and scalability of RF-Bouncer.** The current version of RF-Bouncer needs to deploy a metasurface for each room, causing a huge cost. Fortunately, its cost can be minimized through mass fabrication. Meanwhile, due to the thin surface nature of metasurface, it can potentially be embedded into the environment (e.g., furniture and walls) to reduce the footprint, promoting its widespread deployment. In addition, since each metasurface has a FoV (i.e.,  $[-60^\circ, 60^\circ]$  for RF-Bouncer’s metasurface), by deploying a metasurface in the public area (e.g., the corridor), we can only use a single metasurface to reflect signal into many rooms, so as to avoid each room requires installing a metasurface.

## 7 Conclusion

We have designed, fabricated, and validated RF-Bouncer, a 2-bit dual-band reflecting metasurface to expand indoor wireless coverage. By encoding the phase shifting values, RF-Bouncer can simultaneously manipulate electromagnetic waves in two ISM bands. In addition, RF-Bouncer is transparent to protocols, so as to support diverse commercial IoT devices. Field study shows that RF-Bouncer can enable 15.4 dB average signal strength improvement.

## Acknowledgment

Thanks the anonymous shepherd and reviewers for their valuable comments. This work is supported in part by National Natural Science Foundation of China under Grants (62272388, 61972316, 62061146001) and the Shaanxi International Science and Technology Cooperation Program (2023-GHZD-04, 2023-GHZD-06).

## References

- [1] Smp1340-040lf. <https://www.skyworksinc.com/Products/Diodes/SMP1340-Series>.
- [2] Omid Abari, Dinesh Bharadia, Austin Duffield, and Dina Katabi. Enabling high-quality untethered virtual reality. In *14th USENIX Symposium on Networked Systems Design and Implementation (NSDI 17)*, pages 531–544, 2017.
- [3] Haider Ali, Laeeq Riaz, Syed Abdul Mannan Kirmani, Shahid A Khan, and M Farhan Shafique. Dual band-stop reconfigurable (switchable) frequency selective surface for wlan applications at 2.4 and 5 ghz. *AEU-International Journal of Electronics and Communications*, 143:154038, 2022.
- [4] Venkat Arun and Hari Balakrishnan. Rfocus: Beamforming using thousands of passive antennas. In *17th USENIX Symposium on Networked Systems Design and Implementation (NSDI 20)*, pages 1047–1061, 2020.
- [5] Constantine A Balanis. *Antenna theory: analysis and design*. John wiley & sons, 2015.
- [6] Ertugrul Basar, Marco Di Renzo, Julien De Rosny, Merouane Debbah, Mohamed-Slim Alouini, and Rui Zhang. Wireless communications through reconfigurable intelligent surfaces. *IEEE ACCESS*, 7:116753–116773, 2019.
- [7] Dinesh Bharadia and Sachin Katti. Fastforward: Fast and constructive full duplex relays. *ACM SIGCOMM Computer Communication Review*, 44(4):199–210, 2014.
- [8] Michael Boyarsky, Timothy Sleasman, Mohammadreza F Imani, Jonah N Gollub, and David R Smith. Electronically steered metasurface antenna. *Scientific reports*, 11(1):1–10, 2021.
- [9] Justin Chan, Changxi Zheng, and Xia Zhou. 3d printing your wireless coverage. In *Proceedings of the 2nd International Workshop on Hot Topics in Wireless*, pages 1–5, 2015.
- [10] Hou-Tong Chen, Antoinette J Taylor, and Nanfang Yu. A review of metasurfaces: physics and applications. *Reports on progress in physics*, 79(7):076401, 2016.
- [11] Kun Woo Cho, Yasaman Ghasempour, and Kyle Jamieson. Towards dual-band reconfigurable metamaterial surfaces for satellite networking. *arXiv preprint arXiv:2206.14939*, 2022.
- [12] Kun Woo Cho, Mohammad H Mazaheri, Jeremy Gummesson, Omid Abari, and Kyle Jamieson. mmwall: A reconfigurable metamaterial surface for mmwave networks. In *Proceedings of the 22nd International Workshop on Mobile Computing Systems and Applications*, pages 119–125, 2021.
- [13] Manideep Dunna, Chi Zhang, Daniel Sievenpiper, and Dinesh Bharadia. Scattermimo: Enabling virtual mimo with smart surfaces. In *Proceedings of the 26th Annual International Conference on Mobile Computing and Networking (MobiCom)*, pages 1–14, 2020.
- [14] Chao Feng, Xinyi Li, Yangfan Zhang, Xiaojing Wang, Liqiong Chang, Fuwei Wang, Xinyu Zhang, and Xiaojiang Chen. Rflens: metasurface-enabled beamforming for iot communication and sensing. In *Proceedings of the 27th Annual International Conference on Mobile Computing and Networking*, pages 587–600, 2021.
- [15] Kai Guo, Qun Zheng, Zhiping Yin, and Zhongyi Guo. Generation of mode-reconfigurable and frequency-adjustable oam beams using dynamic reflective metasurface. *IEEE Access*, 8:75523–75529, 2020.
- [16] Sihui Han and Kang G Shin. Enhancing wireless performance using reflectors. In *IEEE INFOCOM 2017-IEEE Conference on Computer Communications*, pages 1–9. IEEE, 2017.
- [17] Hui-Hsin Hsiao, Cheng Hung Chu, and Din Ping Tsai. Fundamentals and applications of metasurfaces. *Small Methods*, 1(4):1600064, 2017.
- [18] Kai-Cheng Hsu, Kate Ching-Ju Lin, and Hung-Yu Wei. Full-duplex delay-and-forward relaying. In *Proceedings of the 17th ACM International Symposium on Mobile Ad Hoc Networking and Computing*, pages 221–230, 2016.
- [19] James R James, Peter S Hall, and Colin Wood. *Microstrip antenna: theory and design*, volume 12. Iet, 1986.
- [20] Wahab Khawaja, Ozgur Ozdemir, Yavuz Yapici, Fatih Erden, and Ismail Guvenc. Coverage enhancement for nlos mmwave links using passive reflectors. *IEEE Open Journal of the Communications Society*, 1:263–281, 2020.
- [21] Girish Kumar and Kamala Prasan Ray. *Broadband microstrip antennas*. Artech house, 2003.
- [22] Teng Li, Hongfu Meng, and Wenbin Dou. Design and implementation of dual-frequency dual-polarization slotted waveguide antenna array for ka-band application. *IEEE Antennas and Wireless Propagation Letters*, 13:1317–1320, 2014.

- [23] Hai Lin, Wen Yu, Rongxin Tang, Jing Jin, Yumei Wang, Jie Xiong, Yanjie Wu, and Junming Zhao. A dual-band reconfigurable intelligent metasurface with beam steering. *Journal of Physics D: Applied Physics*, 55(24):245002, 2022.
- [24] Allen Miu, Hari Balakrishnan, and Can Emre Koksal. Improving loss resilience with multi-radio diversity in wireless networks. In *Proceedings of the 11th annual international conference on Mobile computing and networking*, pages 16–30, 2005.
- [25] Rohan Murty, Jitendra Padhye, Ranveer Chandra, Alec Wolman, and Brian Zill. Designing high performance enterprise wi-fi networks. In *NSDI*, volume 8, pages 73–88, 2008.
- [26] Binh Duong Nguyen and Christian Pichot. Unit-cell loaded with pin diodes for 1-bit linearly polarized reconfigurable transmitarrays. *IEEE Antennas and Wireless Propagation Letters*, 18(1):98–102, 2018.
- [27] Zhangyou Peng, Linxiao Li, Miao Wang, Zhonghao Zhang, Qi Liu, Yang Liu, and Ruoran Liu. An effective coverage scheme with passive-reflectors for urban millimeter-wave communication. *IEEE Antennas and Wireless Propagation Letters*, 15:398–401, 2015.
- [28] Kun Qian, Lulu Yao, Xinyu Zhang, and Tina Ng. Milimirror: 3d printed reflecting surface for millimeter-wave coverage expansion. In *Proceedings of the 28th Annual International Conference on Mobile Computing and Networking*, 2022.
- [29] Hariharan Rahul, Haitham Hassanieh, and Dina Katabi. Sourcesync: A distributed wireless architecture for exploiting sender diversity. *ACM SIGCOMM Computer Communication Review*, 40(4):171–182, 2010.
- [30] Marco Di Renzo, Merouane Debbah, Dinh-Thuy Phan-Huy, Alessio Zappone, Mohamed-Slim Alouini, Chau Yuen, Vincenzo Sciancalepore, George C Alexandropoulos, Jakob Hoydis, Haris Gacanin, et al. Smart radio environments empowered by reconfigurable ai metasurfaces: An idea whose time has come. *EURASIP Journal on Wireless Communications and Networking*, 2019(1):1–20, 2019.
- [31] Yasir Saifullah, Qinzhuo Chen, Guo-Min Yang, Abu Bakar Waqas, and Feng Xu. Dual-band multi-bit programmable reflective metasurface unit cell: design and experiment. *Optics Express*, 29(2):2658–2668, 2021.
- [32] Amin Tayebi, Junyan Tang, Pavel Roy Paladhi, Lalita Udma, Satish S Udma, and Edward J Rothwell. Dynamic beam shaping using a dual-band electronically tunable reflectarray antenna. *IEEE Transactions on Antennas and Propagation*, 63(10):4534–4539, 2015.
- [33] Darrell Whitley. A genetic algorithm tutorial. *Statistics and computing*, 4(2):65–85, 1994.
- [34] Grace R Woo, Pouya Kheradpour, Dawei Shen, and Dina Katabi. Beyond the bits: cooperative packet recovery using physical layer information. In *Proceedings of the 13th annual ACM international conference on Mobile computing and networking*, pages 147–158, 2007.
- [35] Qingqing Wu and Rui Zhang. Towards smart and reconfigurable environment: Intelligent reflecting surface aided wireless network. *IEEE Communications Magazine*, 58(1):106–112, 2019.
- [36] Xi Xiong, Justin Chan, Ethan Yu, Nisha Kumari, Ardalan Amiri Sani, Changxi Zheng, and Xia Zhou. Customizing indoor wireless coverage via 3d-fabricated reflectors. In *Proceedings of the 4th ACM International Conference on Systems for Energy-Efficient Built Environments*, pages 1–10, 2017.
- [37] Hongjing Xu, Shenheng Xu, Fan Yang, and Maokun Li. Design and experiment of a dual-band 1 bit reconfigurable reflectarray antenna with independent large-angle beam scanning capability. *IEEE Antennas and Wireless Propagation Letters*, 19(11):1896–1900, 2020.
- [38] Fan Yang, Ruyuan Deng, Shenheng Xu, and Maokun Li. Design and experiment of a near-zero-thickness high-gain transmit-reflect-array antenna using anisotropic metasurface. *IEEE transactions on antennas and propagation*, 66(6):2853–2861, 2018.
- [39] R Ivan Zelaya, William Sussman, Jeremy Gummesson, Kyle Jamieson, and Wenjun Hu. Lava: fine-grained 3d indoor wireless coverage for small iot devices. In *Proceedings of the 2021 ACM SIGCOMM 2021 Conference*, pages 123–136, 2021.
- [40] Lei Zhang, Ming Zheng Chen, Wankai Tang, Jun Yan Dai, Long Miao, Xiao Yang Zhou, Shi Jin, Qiang Cheng, and Tie Jun Cui. A wireless communication scheme based on space-and frequency-division multiplexing using digital metasurfaces. *Nature electronics*, 4(3):218–227, 2021.
- [41] Lei Zhang, Xiao Qing Chen, Shuo Liu, Qian Zhang, Jie Zhao, Jun Yan Dai, Guo Dong Bai, Xiang Wan, Qiang Cheng, Giuseppe Castaldi, et al. Space-time-coding digital metasurfaces. *Nature communications*, 9(1):1–11, 2018.
- [42] Na Zhang, Ke Chen, Yilin Zheng, Qi Hu, Kai Qu, Junming Zhao, Jian Wang, and Yijun Feng. Programmable coding metasurface for dual-band independent real-time

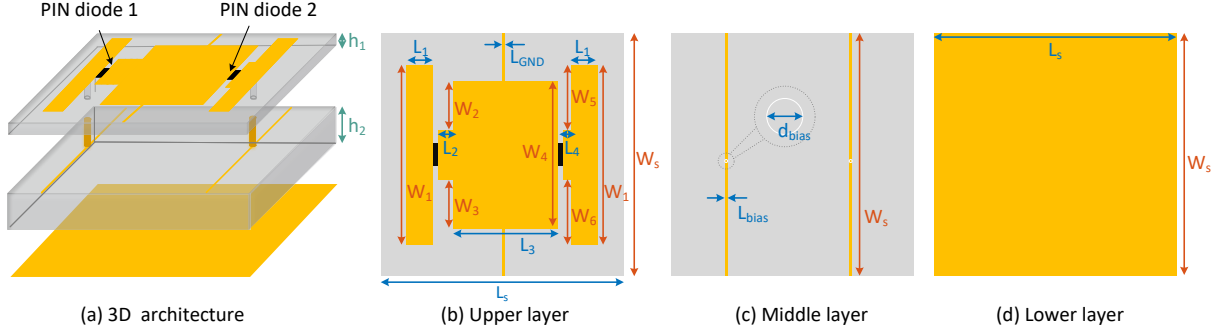


Figure 35: The structure of optimal unit-cell.

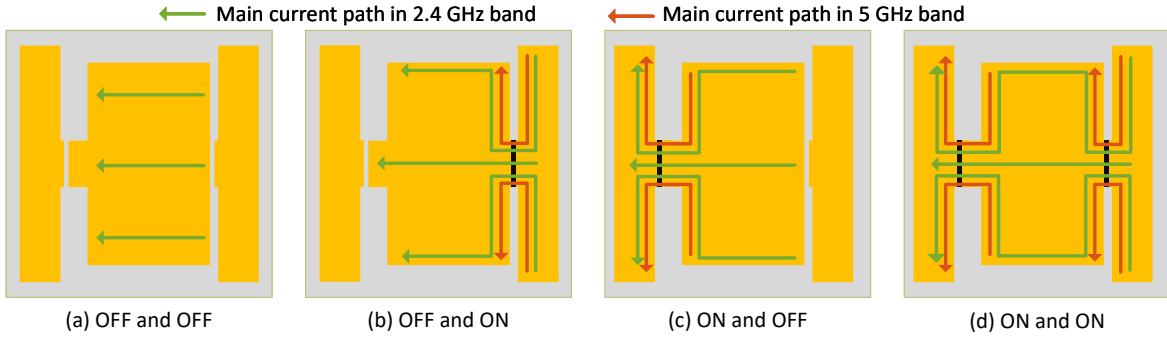


Figure 36: The meta-atom as a 2-bit phase shifter.

beam control. *IEEE Journal on Emerging and Selected Topics in Circuits and Systems*, 10(1):20–28, 2020.

## A Appendix

Figure 35 illustrates the structure of optimal unit-cell and Table 2 summarizes the optimal unit-cell parameter configurations. We place two PIN diodes with the opposite orientation on the upper patch layer as shown in Figure 35(b). The bias current supported by a DC voltage regulator flows from the bias line and flows to the patch through two vertical via-holes. Then, it flows to the GND line after passing through PIN diodes. Under the different DC voltage levels, each PIN diode switches to “ON” or “OFF” state and thus the opening directions of each patch have four states, as shown in Figure 36. Depending on the sign of the bias current, the meta-atom introduces a phase shifting of  $0, \pi/2, \pi$ , or  $3\pi/2$ . In addition, in order to decouple the influence between each bias line, we partition the whole metasurface into 4 areas (e.g., A, B, C,

and D in Figure 13), so the maximum number of bias lines passing through a unit-cell is reduced from 16 to 8.

Therefore, we can consider the meta-atom as a 2-bit phase shifter, corresponding to four electromagnetic responses. In order to independently adjust each meta-atom’s phase, we employ a bias line layer to control the states of the PIN diode within each meta-atom.

Table 2: The parameters of the unit-cell.

Parameter	Value (mm)	Parameter	Value (mm)
$L_s$	19.5	$W_s$	19.5
$L_1$	3	$L_2$	1.4
$L_3$	9.1	$L_4$	0.2
$L_{bias}$	0.2	$L_{GND}$	0.4
$W_1$	17.5	$W_2$	5.8
$W_3$	5.8	$W_4$	15
$W_5$	7	$W_6$	7
$h_1$	0.3	$h_2$	6.5
$d_{bias}$	0.8		